HAL
open science

Retrieving CeB 6 's lost magnetic entropy

Mehdi Amara, Christine Opagiste, Rose-Marie Galéra

To cite this version:

Mehdi Amara, Christine Opagiste, Rose-Marie Galéra. Retrieving CeB 6 's lost magnetic entropy. Physical Review B, 2020, 101 (9), pp.094411. 10.1103/PhysRevB.101.094411 . hal-02863867

HAL Id: hal-02863867

https://hal.science/hal-02863867v1

Submitted on 10 Jun 2020

HAL is a multi-disciplinary open access archive for the deposit and dissemination of scientific research documents, whether they are published or not. The documents may come from teaching and research institutions in France or abroad, or from public or private research centers.

L'archive ouverte pluridisciplinaire **HAL**, est destinée au dépôt et à la diffusion de documents scientifiques de niveau recherche, publiés ou non, émanant des établissements d'enseignement et de recherche français ou étrangers, des laboratoires publics ou privés.

Retrieving CeB_6's lost magnetic entropy

Mehdi Amara,* Christine Opagiste, and Rose-Marie Galéra
Université Grenoble Alpes, CNRS, Grenoble INP, Institut Néel, 38000 Grenoble, France

(Received 12 July 2019; revised manuscript received 20 December 2019; accepted 24 February 2020; published 11 March 2020)

The reported temperature variations of CeB_6's magnetic entropy are inconsistent with the fourfold degeneracy of the crystal field ground state. This old question is here addressed through new specific heat measurements and an improved description, in the cage context, of both the phonons and crystal field contributions to the specific heat. The antiferromagnetic transition is characterized as first order and its latent heat determined. From the phonons' dispersion for a cage compound, the lattice specific heat contribution is derived from the LaB_6 data. Once corrected for the first-order transition and lattice contributions, the magnetic entropy displays the characteristic plateau of the quadruplet crystal field ground state, but at temperatures in excess of 30 K. Below 30 K, as the ordering temperature is approached, the magnetic entropy is substantially reduced. This anomalous temperature dependence is consistent with a crystal field ground state split by the rare-earth movement, a phenomenon specific to rare-earth cage compounds.

DOI: 10.1103/PhysRevB.101.094411

I. INTRODUCTION

For decades, the CeB_6 compound has been a center of interest in the fields of unconventional magnetism and heavy fermions physics. At low temperature and under zero magnetic field, it undergoes two orderings: From the paramagnetic state (phase I), an ordered state (phase II) develops at $T_Q = 3.3$ K, then, at $T_N = 2.3$ K, an antiferromagnetic state (phase III) is stabilized [1–3]. Between T_N and T_Q, within phase II, the ordered state is reported to be nonmagnetic and frequently interpreted as an antiferroquadrupolar order [4,5], i.e., an order where $4f$ electric quadrupoles alternate from site to site. However, this interpretation is difficult to reconcile with a number of observations [6,7]. Beside the difficulties in the interpretation of the properties of this ordered state, the paramagnetic phase itself is not devoid of puzzles. There, the strong couplings of the $4f$ electron with the conduction electrons and its lattice environment are already manifest. The measurements show a Kondo-like resistivity minimum around 150 K [2,8] and a large contribution of the conduction electrons to the magnetic susceptibility, which result in a reduction of the apparent Ce^{3+} magnetic moment [1,9]. Moreover, the strength of the cubic crystalline electric field (CEF) is unusually large: Inelastic neutron (INS) and Raman scatterings show that the $J = 5/2$ multiplet is split with a 540 K separation between the Γ_7 doublet and Γ_8 quadruplet [10]. From the magnetic entropy variations, derived from specific heat measurements [11,12], the possibility of a Γ_7 doublet CEF ground state can be discarded. Although the reported values at $T_Q = 3.3$ K are close to the $R\ln 2$ J/(K mol) value of a doublet [11–13], the magnetic entropy steadily increases in the paramagnetic range, rapidly exceeding the doublet value. This variation is, however, hardly consistent with a quadruplet ground state: The quadruplet value is not reached below 40 K and no plateau, characteristic of a well isolated ground state, is to be observed. Also, the reported entropy value at T_Q, close to $R\ln 2$, is challenging the interpretation of phase II as a nonmagnetic state. Indeed, according to the Kramers theorem applied to the Ce^{3+} case, the minimal magnetic entropy within a nonmagnetic state is precisely $R\ln 2$ J/(K mol). Starting from such an already reduced entropy, how is it then possible for the CeB_6 system to undergo, first, a nonmagnetic transition and, second, an antiferromagnetic one? A better understanding of the physical mechanisms at play in CeB_6 requires clarifying this paramagnetic entropy issue. In the work introduced here, this question is addressed thanks to improvements along three directions: The experimental determination of the specific heat, the description of the phonons' contribution to the specific heat, and the theory in order to account for the specific CEF effects in the cage context.

II. EXPERIMENTAL DETERMINATION OF THE MAGNETIC ENTROPY

A. Specific heat measurements

In order to improve the experimental determination of the magnetic entropy of CeB_6, new specific heat measurements were performed. As regards the LaB_6, nonmagnetic reference, single crystals grown in Kiev, by the team of Dr. N. Shitsevalova, were used. These crystals were obtained from borothermal reduction of La_2O_3, under vacuum at 1750 °C, using amorphous natural boron. The obtained powder was successively pressed into rods and sintered at 1800 °C. The rods were then processed by zone melting under argon atmosphere [14], resulting in large, single phase, LaB_6 crystals. The used CeB_6 crystals are from older batches, similarly processed [15] in Sendai by Professor S. Kunii. They were lent to us by Dr. L. P. Regnault. These high-quality single crystals, initially intended for neutron scattering experiments, were produced using ^{11}B enriched boron, whereas natural boron

*mehdi.amara@neel.cnrs.fr

 ©2020 American Physical Society

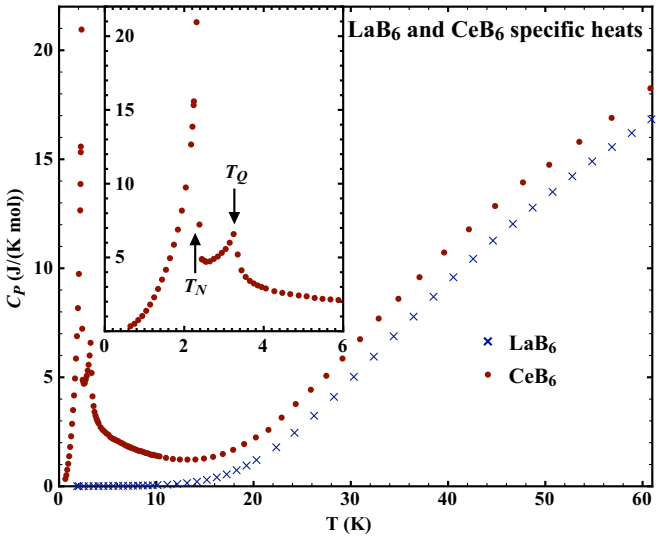

FIG. 1. The temperature dependence of the specific heat for LaB_6 (crosses) and CeB_6 (round dots), as determined using the relaxation technique. The inset gives the low temperature detail for CeB_6, showing the transitions at T_N and T_Q. Note the very sharp anomaly at T_N.

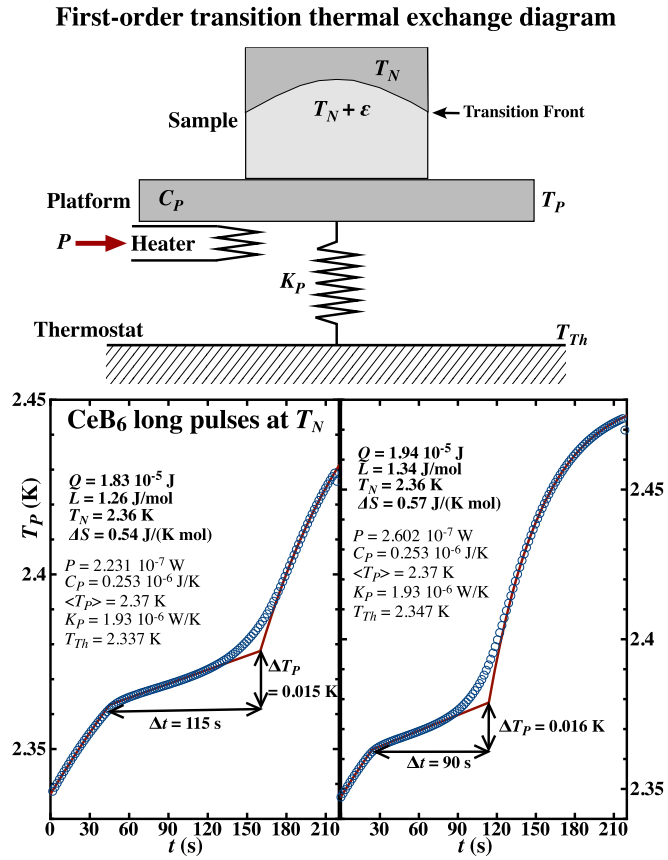

FIG. 2. Upper part: Thermal exchange scheme during a first-order transition in heating conditions. The sample's platform has heat capacity C_P, thermal resistance to the thermostat K_P, and absorbs a heating power P. As the transition front moves, instead of being constant, the platform temperature T_P increases. Lower part: Two examples of $T_P(t)$ temperature profiles, showing the crossing of the antiferromagnetic transition in CeB_6, when using long heating pulses. These processes have the same duration but differ in their starting temperature and temperature rise (related to the heating power P). The full lines are adjusted considering exponential relaxation laws above and below a linear plateau of duration Δt and temperature rise ΔT_P.

was used for our LaB_6 reference. All the used crystals were received in the form of oriented platelets. The small specific heat samples of masses $m = 6$ mg for LaB_6 and $m = 2.95$ mg for CeB_6, were subsequently cut from these. The specific heat measurements were performed using the relaxation technique in an automated [16] Quantum Design PPMS system. Two cryogenic configurations were used, the normal ^{4}He flux one, for temperatures between 1.8 and 60 K, and the additional closed-cycle ^{3}He insert for temperatures down to 0.6 K (in the case of CeB_6 only). The thermal coupling between the sample and the setup platform was improved by use of a very small quantity of Apiezon N grease, which is accounted for thanks to the addenda measurements.

The LaB_6, nonmagnetic reference curve (see Fig. 1), was obtained using the default two time constants (two-tau) fitting of the relaxation process, as provided by the PPMS software. The same options were used for the CeB_6 sample, but this time using the ^{3}He insert. Figure 1 shows the resulting specific heat curve for CeB_6. Inspecting the collected data for CeB_6, it appeared that the two-tau fitting was systematically failing at the top of the antiferromagnetic anomaly at T_N. As shown in Fig. 1, the processed relaxation data display a very sharp anomaly at T_N, in agreement with the literature. This aspect of the anomaly and the failure of the fitting process at T_N, made us suspect a first-order antiferromagnetic transition. To clarify this point, a second series of measurements on the same sample, using the standard ^{4}He setup, was carried out, focusing on the transition at T_N. This time, the system was forced to proceed by using long heating pulses, with adjusted duration and temperature amplitude, which affect the heating power, in order to cover the whole transition process. The lower part of Fig. 2 shows two examples of time dependence of the platform temperature, for long pulses processes crossing the antiferromagnetic transition. The inflection in the temperature evolution that reflects the expected first-order plateau at T_N, is well evidenced. The "plateau" actually displays a significant slope, which can be understood considering that the sample cannot be of uniform temperature (see the thermal exchange diagram of Fig. 2, upper part): As the transition front moves through the sample, the platform temperature keeps increasing, but at a slower pace, until the "cold" point at T_N disappears with the last fraction of antiferromagnetic CeB_6. The difficulty then lies in defining the duration Δt of the transition and the corresponding temperature rise ΔT_P of the platform. This is done here by idealizing the temperature profile during the transition, replaced by a constant slope process. The curves before and after the plateau can be fitted with simple relaxation exponentials, with identical temperature limit, but different time constants due to different sample specific heat above and below the transition. The process is analyzed considering only conductive heat exchange (coupling constant K_P between the platform and the thermostat), a stable

thermostat at temperature T_{Th}, and constant heating power P. During the transition process, the heat absorbed by the sample is

$$Q = [P - K_P(\langle T_P\rangle - T_{\mathrm{Th}})]\Delta t - C_P \Delta T_P,$$

where $\langle T_P\rangle$ is the time averaged temperature of the platform during the process and C_P is the platform heat capacity (including the thermal contact grease). For a good coupling between the platform and sample, the same temperature rise ΔT_P will occur at the sample's face in contact with the platform. As the sample's fraction that has not undergone the transition maintains a T_N temperature, there is a thermal gradient between the transition front and the platform (Fig. 2, upper part). At the end of the process, when the last fraction at T_N disappears, the sample is, on average, overheating with respect to T_N. In the simplest case of a linear temperature profile and a regular sample's shape, the sample's average temperature is then close to $(T_P + T_N)/2$. This means that the extent of the overheating with respect to T_N is $(T_P - T_N)/2 = \Delta T_P/2$. In the definition of the latent heat L of the transition, one can account for this excess of heat transfer to the sample:

$$L = Q - C_S(T_{N_+})\frac{\Delta T_P}{2},$$

where $C_S(T_{N_+})$ is the sample specific heat immediately above the transition temperature. Using the thermal parameters of the PPMS "puck" (see Fig. 2), averaging the values derived from the two pulses and estimating the uncertainty on such a determination as not better than 10%, one obtains

$$L = 1.30 \pm 0.13\ \mathrm{J/mol}.$$

The corresponding change in entropy for the transition at $T_N = 2.36$ K is

$$\Delta S = L/T_N = 0.55 \pm 0.06\ \mathrm{J/(K\,mol)}.$$

The characterization of the antiferromagnetic transition as first order allows us to recover some of the missing paramagnetic entropy of CeB_6. This correction represents about 5% of the entropy of a quadruplet ground state.

B. Phonons' contribution to the specific heat

At this point, the remaining difficulty for extracting the magnetic part of the specific heat, then the magnetic entropy of CeB_6, is the proper identification of the nonmagnetic contributions. This requires determining the temperature dependence of the specific heat for a nonmagnetic element in the series, in the present case LaB_6. In a nonmagnetic metal, the specific heat C is usually well described by separating two contributions, one from the conduction electrons C_e, and the other from the phonons C_{ph}:

$$C(T) = C_e(T) + C_{\mathrm{ph}}(T). \tag{1}$$

Due to the very low compressibility of solids, no distinction is made here between the constant pressure and the constant volume specific heat. At low temperature, where it is influent, the electronic term can be reduced to the linear form $C_e(T) = \gamma T$, where γ is the specific heat electronic constant. As regards the phonon term C_{ph}, the most common approach is to describe it using the Debye approximation which, in the low temperature limit, yields the cubic temperature term. This term reflects the low frequency acoustic modes and, in principles, allows deriving, from a nonmagnetic reference, the phonons contribution for a magnetic element in the series. In the simplest harmonic approach, the forces that determine the springs stiffnesses in a classical model are maintained, whereas the inertia increases across the series. In this scheme, the eigenfrequencies, as well as the Debye temperature, scale via the square root of the formula masses ratio. If necessary, more than one Debye temperature are introduced [17]. This Debye approach is known to fail in the description of cage compounds, where the low temperature dependence of the phonon specific heat cannot be reduced to a cubic term. In these systems, the weakly dispersive rattling of the cage guest yields contributions closer to the Einstein approach than to the dispersive (acoustic) Debye one. In the case of rare-earth hexaborides, there has been attempts [18–20] at describing the phonon contribution by using the Einstein model or an empirical mixture of Einstein and Debye. This increases the number of involved parameters and, by lack of an underlying physical model, it is difficult to scale them from one element to another in the series.

1. Phonons dispersion in a cage system

In light rare-earth hexaborides, the two lowest phonon dispersion branches are well reproduced by a harmonic model consisting of a chain, of period d, of identical rigid cages of masses M (see the upper part of Fig. 3), interconnected by springs of stiffness K_0 (see Ref. [21]). In each cage a mass m, the rare earth, is attached by a spring of stiffness k_0. Writing the classical equations of motion for small deviations from the equilibrium positions along the chain axis, introducing a propagating wave at frequency ω and wave vector q (in reduced unit, with $q = 0.5$ at the zone border), one obtains the relation

$$\cos(2\pi q) = 1 - 2\left(1 + \frac{m}{M}\frac{{\omega_0}^2}{{\omega_0}^2 - \omega^2}\right)\frac{\omega^2}{{\Omega_0}^2}, \tag{2}$$

where ${\omega_0}^2 = k_0/m$ is the natural frequency of the "rattler" and ${\Omega_0}^2 = 4K_0/M$ is the top acoustic frequency for a chain of empty cages. This allows defining the two branches of the dispersion curves, here written by introducing $x = \omega/\omega_0$, the mass ratio $\alpha = m/M$, the frequency ratio $\rho = \Omega_0/\omega_0$, and the function $K(q) = \rho^2[1 - \cos(2\pi q)]/2$:

$$\omega_\pm(q) = \omega_0\sqrt{\frac{1 + \alpha + K(q) \pm \sqrt{[1 + \alpha + K(q)]^2 - 4K(q)}}{2}}, \tag{3}$$

where the + and − options, respectively, give the expression for the optical and acoustic branches.

Figure 3 shows the dispersion curves for longitudinal waves propagating along [0 0 q] in LaB_6 (from Ref. [18]) and CeB_6 (from Ref. [19]). These dispersion curves have three characteristic points, at positions Γ and X in the cubic first Brillouin zone (see Fig. 4), that allow a direct determination of the parameters ω_0 and Ω_0: (i) the $q = 0$ point (Γ point of the cubic zone), where all the optical branches at the energy $E^\Gamma = \hbar\omega_+(0)$ converge. From Eq. (2), $\omega_+(0) = \omega_0\sqrt{1+\alpha}$.

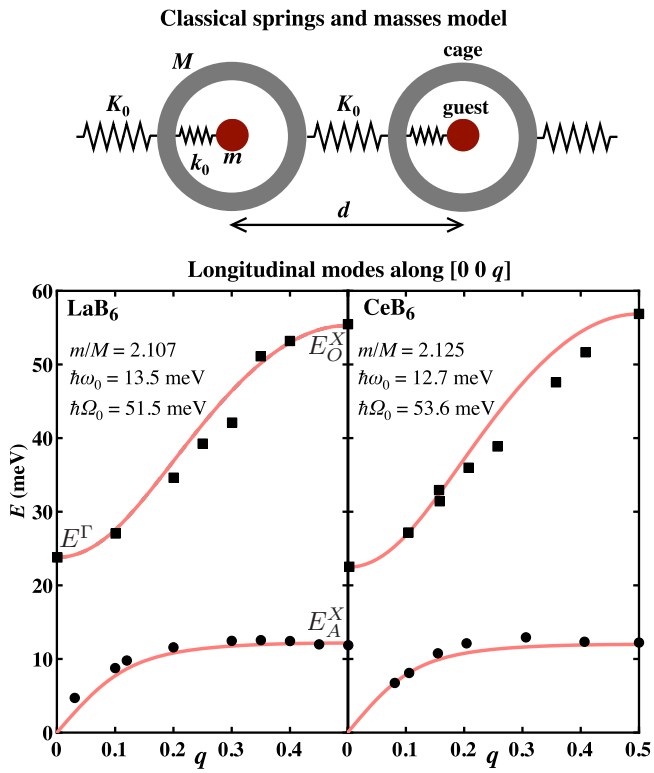

FIG. 3. Upper part: The chain of masses (m for the guest and M for the cage) and springs (stiffnesses k_0, K_0) used for the harmonic, classical description of lattice modes in a cage system. Lower part: The inelastic neutron scattering data for LaB_6 (left, from Ref. [18]) and CeB_6 (right, from Ref. [19]), showing the dispersion of the longitudinal mode along the fourfold direction. Superimposed are the dispersions curves (full lines) derived from the above model for the indicated values of mass ratios and frequencies.

Using the mass ratios α for 98% enriched boron, one obtains $\hbar\omega_0 = 13.5$ meV for LaB_6 and $\hbar\omega_0 = 12.7$ meV for CeB_6. (ii) The zone border $q = 1/2$ (X point in the [0 0 q] direction), for the acoustic and optical branches, respectively yielding the energies E_A^X and E_O^X. From Eq. (2), one can identify the frequency Ω_0 for these longitudinal waves: $\hbar^2\Omega_0{}^2 = (E_A^X)^2 + (E_O^X)^2 - (E^\Gamma)^2$. In this way, one obtains $\hbar\Omega_0 = 51.5$ meV for LaB_6 and $\hbar\Omega_0 = 53.7$ meV for CeB_6. However, caution is required as regards the precision of these determinations. The used dispersion curves were obtained from inelastic neutron scattering on triple axis spectrometers. In such conditions, the error on an energy determination can exceed 1%. Using the above values, computed curves are superimposed on the experimental data in Fig. 3. The agreement is very satisfactory considering the above evoked uncertainties and the simplicity of the model, dependent on only two parameters.

For small deviations from the equilibrium positions, the motion equations that yield Eq. (2) for a chain generalize to a three-dimensional lattice. One has to replace the (cage+guest) element in the chain by an infinite plane of these same elements, perpendicular to the wave vector. Within this plane, all cages, respectively guests, share the same deviation. For a given polarization, two variables are sufficient to describe the parallel deviations, one for the cages and the other for the guests. The problem is then formally identical to the single-dimensional one and, to adapt the chain's equations, one only needs to consider the relevant period d, along the wave vector direction $\widehat{\mathbf{q}}$, and stiffnesses appropriate to the polarization direction $\widehat{\mathbf{p}}$. The period d that has to be considered is the smallest spacing between consecutive lattice planes perpendicular to $\widehat{\mathbf{q}}$. This minimal spacing defines the smallest, physically relevant wavelength on the lattice $\lambda = 2d$, which, in the reciprocal space, is associated with the first zone border vector $\mathbf{B_q}$, parallel with $\mathbf{q}$. On the segment from the origin to $\mathbf{B_q}$, the dispersion relations keep the forms of Eq. (2), provided one replaces $\cos(2\pi q)$ with $\cos(\pi\frac{|\mathbf{q}|}{|\mathbf{B_q}|})$ and defines $K(q)$ as $K(q) = \rho^2[1 - \cos(\pi\frac{|\mathbf{q}|}{|\mathbf{B_q}|})]$ in Eq. (3). As the frequency ω_0, and its associated k_0 stiffness, are isotropic in a cage with O_h symmetry, they apply for all wave vectors and polarizations. In the generalization of the dispersion relation, only the top frequency Ω_0, for the lattice of empty cages, has to be adapted to the wave polarization $\widehat{\mathbf{p}}$ and propagation direction $\widehat{\mathbf{q}}$, replacing the constant Ω_0 with the function $\Omega_0(\widehat{\mathbf{q}}, \widehat{\mathbf{p}})$ in Eq. (2). In search for a simplification, it is assumed that using a constant $\widetilde{\Omega}_0$, in place of the function $\Omega_0(\widehat{\mathbf{q}}, \widehat{\mathbf{p}})$, can result in a satisfactory description of the low temperature specific heat of a hexaboride. This is inspired by the Debye approximation, but provides a more realistic description of the cage context: The characteristic features of the dispersion curves, in particular the flattened acoustic branch surmounted by an energy gap, are preserved. In this way, only two parameters are required for the description of the phonons's contribution: The rattler frequency ω_0 and $\widetilde{\Omega}_0$. The parameter $\widetilde{\Omega}_0$ represents an averaged lattice of empty boron cages. As such, it should not vary much across the RB_6 series, except for the anharmonic effect of a slight reduction in the lattice parameter due to the lanthanide contraction.

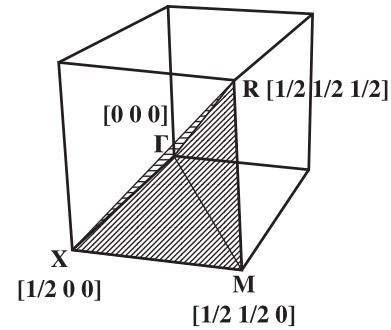

FIG. 4. The positive octant of the cubic's first Brillouin zone showing the characteristic points Γ, X, M, and R. These points are the vertices of a tetrahedron (hatched faces) that, under the cubic transformations, generates the whole first Brillouin zone. In the numerical calculation of the phonons' specific heat, all the considered samples belong to this representative volume.

2. *Cage system specific heat*

Thanks to the above simplification, for any $\mathbf{q}$ within the first Brillouin zone, one can associate two frequencies $\tilde{\omega}_\pm(\mathbf{q})$. Using the polarization independent average $\widetilde{\Omega}_0$, in place of $\Omega_0(\widehat{\mathbf{q}}, \widehat{\mathbf{p}})$, the same frequency applies for the longitudinal and transverse modes. Then, at temperature T, the phonons

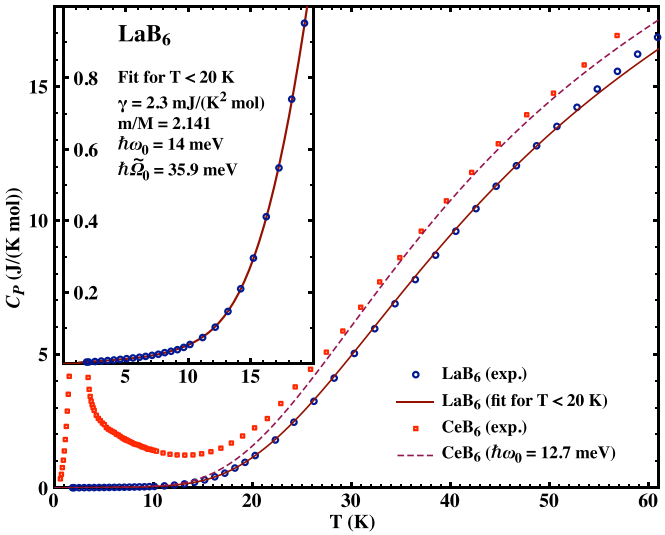

FIG. 5. The specific heat for LaB_6 (circles) and CeB_6 (squares) confronted with calculations based on the generalized dispersion curves and including the electronic term (defined by the γ constant). The full lines show the computed curves for LaB_6, using ω_0 and $\widetilde{\Omega}_0$ values deduced from a fit below 20 K (see details and values in the inset). The dashed line is an attempt at describing the nonmagnetic background of CeB_6 using the neutron data for ω_0 and a $\widetilde{\Omega}_0$ value derived from the LaB_6 fit.

specific heat $C_{\rm ph}$ can be computed by summing, within the first Brillouin zone, over all wave vectors and polarizations describing the vibration modes:

$$C_{\rm ph}(T) = 3\sum_{\mathbf{q},\pm} k_{\rm B}\left(\frac{\hbar\,\tilde{\omega}_{\pm}(\mathbf{q})}{k_{\rm B}T}\right)^2 \frac{e^{-\frac{\hbar\,\tilde{\omega}_{\pm}(\mathbf{q})}{k_{\rm B}T}}}{\left(1-e^{-\frac{\hbar\,\tilde{\omega}_{\pm}(\mathbf{q})}{k_{\rm B}T}}\right)^2}, \quad (4)$$

where the factor 3 accounts for the three polarizations and the sum runs over all wave vectors $\mathbf{q}$ and associated frequencies ($\pm$). In practice, the summation can be performed for a discrete fraction of the first Brillouin zone, considering, inside the positive octant, samples at a number N of $\mathbf{q}$ nodes on a cubic lattice. In direct space, this amounts to the calculation of the specific heat for a crystal consisting of N unit cells. Obviously N needs to be large enough to approach the macroscopic limit. This requirement can substantially slow down the calculation and it is preferable to take advantage of the cubic symmetry. Redundant contributions can be avoided by restricting to nodes included in a representative polyhedron as represented in Fig. 4: Each considered $\mathbf{q}$ node accounts for its symmetry equivalents by considering a multiplicity factor. In Fig. 5 this method of calculation is used for describing the LaB_6 experimental data. The displayed curves are computed considering 364×3 representative samples of the first Brillouin zone, equivalent to 1728×3 modes in the positive octant. At the graph's scale, calculations for as few as 56×3 representative samples are indistinguishable from the displayed curves. The electronic term is deduced from the linear, low temperature part of the curve. As regards the phonons contribution, only two parameters are active, ω_0 and $\widetilde{\Omega}_0$, for adjusting the computed curve to the experimental data. The values appearing in Fig. 5 are obtained by a mean-square fit on the data for temperatures lower than 20 K (inset of Fig. 5). The calculated curves, based on the low temperature data, extrapolate very well up to 50 K. Above 50 K, the cost of the simplification of the dispersion curves, here adapted to the low temperature specific heat, starts to materialize: A better description in this temperature range would require increasing the $\widetilde{\Omega}_0$ value. Looking at the refined values for ω_0 (reported in Fig. 5), $\hbar\omega_0 = 14$ meV is larger than the inelastic neutron scattering determination at 13.5 meV, but the difference may be within the uncertainty of the neutron determination (which values are not explicit in Refs. [18,19]). In order to adapt the phonon contribution from the LaB_6 reference to the CeB_6 case, one can think of resorting to a mass scaling in the harmonic model context. This is done in the hypothesis that the underlying forces, resulting in the stiffnesses of the elastic description, are maintained in CeB_6. Then, one should correct the eigenfrequencies by a factor reflecting the ratios of the atomic masses, $\sqrt{\frac{M_{\rm La}}{M_{\rm Ce}}}$ for ω_0, and $\sqrt{\frac{M_{\rm B_{nat.}}}{M_{\rm B_{enr.}}}}$ for $\widetilde{\Omega}_0$. The later correction is required in order to account for the use of natural boron ($B_{\rm nat.}$) in the synthesis of LaB_6 as opposed to 98% ^{11}B enriched boron in the case of CeB_6 ($B_{\rm enr.}$). One thus derives the following values for the phonons' contribution parameters in CeB_6: $m/M = 2.125$, $\hbar\omega_0 = 13.9$ meV, and $\hbar\widetilde{\Omega}_0 = 35.6$ meV. This mass scaling has a tiny effect, resulting in a curve almost undistinguishable from that of LaB_6 at the scale of Fig. 5. It cannot account, even in the presence of magnetic effects, for the specific heat difference observed above 20 K between the CeB_6 and LaB_6 curves of Fig. 1. The failure of the mass scaling points to the limits of the harmonic approximation, despite its seemingly satisfactory description of the dispersions. In particular, the cage context implies large amplitude excursions for the rare earth within the rigid limits of the cage. This alone would determine an anharmonic potential, even in the absence of magnetic effects, as it implies a sharply rising potential close to the boron framework. In the simplest picture, one can expect the smaller Ce^{3+} ion to have more room than La^{3+}, which, independently of the mass correction, would result in a lower ω_0 frequency for CeB_6.

As regards the ω_0 value for CeB_6, a more empirical option is the neutron spectroscopy determination of $\hbar\omega_0$ that yields 12.7 meV. In the hypothesis that the harmonic correction can still be applied to the rigid boron framework, where small deviations from the equilibrium position are granted, the mass scaled value for $\widetilde{\Omega}_0$ is maintained. This defines a second set for the parameters defining the CeB_6 nonmagnetic contribution: $m/M = 2.125$, $\hbar\omega_0 = 12.7$ meV, and $\hbar\widetilde{\Omega}_0 = 35.6$ meV. This time, the corresponding curve in Fig. 5 is much closer to the CeB_6 data (dashed line for $\hbar\omega_0 = 12.7$ meV). This supports the idea that the large difference in the background specific heat, with respect to the LaB_6 reference, is essentially due to the frequency ω_0 of the guest inside the cage. Indeed, in the temperature range of interest, the computed curve is very sensitive to the ω_0 value. Considering the uncertainty on the neutron scattering data, and the 0.5 meV discrepancy observed in the LaB_6 case, the agreement of $\hbar\omega_0 = 12.7$ meV with the CeB_6 background is somewhat lucky. Note that the value used for the γ electronic constant, of little influence above 20 K, is the same as the one derived from the LaB_6 low temperature data (inset of Fig. 5).

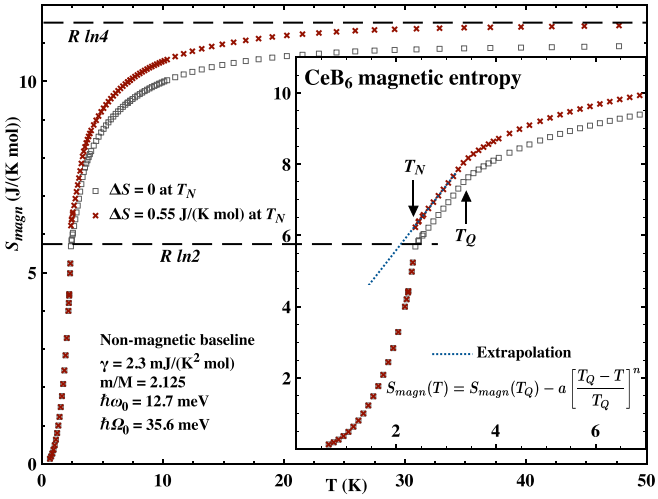

FIG. 6. Temperature variation of CeB_6 magnetic entropy. The cross and square symbols, respectively, show data corrected, or uncorrected, for the first-order transition at T_N. The inset gives the detail of this variation for $T < 10$ K. All curves are corrected for the nonmagnetic contributions to the specific heat (computed using the displayed parameters). The dashed horizontal lines refer to the entropy values for a doublet ($R\ln 2$) and a quadruplet ($R\ln 4$). The dotted line in the inset is a least-squares fit to the corrected data in phase II, using the displayed expression for $S_{\rm mag}(T_Q) = 8.101$ J/(K mol), $T_Q = 3.38$ K, $a = -6.066$ J/(K mol), and $n = 0.983$.

C. The magnetic entropy of CeB_6

Despite the uncertainty on the ω_0 value, the computed curve for CeB_6 in Fig. 5 provides a likely nonmagnetic background. One can then proceed with the determination of the magnetic entropy of CeB_6 by subtracting this background from the specific heat in order to define the magnetic contribution $C_{\rm mag}(T)$. Between zero temperature and 0.6 K, the missing CeB_6 specific heat data are extrapolated using a power-law fit on the data between 0.6 K and T_N. Integrating $C_{\rm mag}\,dT/T$ from 0 to the current temperature, shifting the values above T_N by the amount of the first-order entropy jump $\Delta S = 0.55$ J/(K mol) (see Sec. II A), one obtains the temperature variation of $S_{\rm mag}(T)$ represented by the cross symbols in Fig. 6. This temperature dependence shows that the paramagnetic entropy plateau, expected for the cubic Γ_8 quadruplet CEF ground state, is recovered at temperatures in excess of 30 K. The uncorrected data (empty squares in Fig. 6) cannot reach the quadruplet value in the graph temperature range. Note that, in agreement with the literature [11–13], the uncorrected value just above T_N is very close to the entropy of a doublet. Although the corrected curve asymptotically approaches the $R\ln 4$ line in Fig. 6, one should remember that this variation is subjected to a number of uncertainties. In addition to the discrete integration errors, the jump in entropy at T_N is defined at no better than 10%, which represents a shift in the 0.1 J/(K mol) range. Moreover, the neutron scattering value $\hbar\omega_0 = 12.7$ meV, of limited precision, is directly responsible for the almost zero slope of $S_{\rm mag}(T)$ above 30 K. Nevertheless, it is shown here that the experiments are consistent with a quadruplet CEF ground state and that the recovery of the fourfold degeneracy entropy is progressive: At T_Q, the entropy is close to 8 J/(K mol) and it takes more than 30 K to retrieve the missing 30% of the quadruplet entropy.

III. ENTROPY OF A CAGE-SPLIT QUADRUPLET

The experiments show that, in the paramagnetic range, the magnetic entropy value just above T_Q is much lower than expected for a quadruplet. It is about $R\ln 2.6$ J/(K mol) against $R\ln 4$ for an effective fourfold degeneracy. This means that the ground-state degeneracy is already largely reduced before any ordering process. Such a premature reduction of the entropy is usually ascribed to pair correlations that precede the actual, long range, ordering. However, in the CeB_6 case, the ordering temperatures T_Q and T_N are one order of magnitude smaller than the thermal amplitude of the paramagnetic entropy variation. This attests to the weakness of the pair couplings that drive the ordering, with respect to the energy scale relevant to the entropy variation. This scale actually fits with another one, highlighted in the Raman and neutron scattering investigation of CeB_6 crystal field scheme [10]. At low temperature, the authors observed an increase in the energy transfer between the Γ_8 ground state and the excited Γ_7 level. They interpreted this as resulting from a split Γ_8 ground state over a 30 K interval, which agrees with the temperature range of the entropy variation. As there is no evidence of a static lattice distortion, the average symmetry of the Ce site remaining cubic, they evoked a possibly dynamic symmetry lowering. This is precisely what can be expected from the large amplitude movement of the rare earth inside its boron cage, if one considers its crystal field consequences [21]. In the following, we apply the general considerations of Ref. [21] to the particular case of CeB_6, with the intent of a quantitative description of the thermodynamic anomalies in the paramagnetic range.

A. Cage crystal field

Due the movement of the rare earth inside the oversized cage, one has to correct the central cubic CEF Hamiltonial $\mathcal{H}_0$. At a position offset by $\boldsymbol{r}$, the CEF Hamiltonian for the Ce^{3+} ion has to include a correction $\mathcal{H}_d(\boldsymbol{r})$. In the frame of the moving rare earth, the corrective term becomes time dependent, thus dynamic. However, from the $4f$ electron perspective, the rare-earth movement is so slow that this correction can be treated as a static one [21] at position $\boldsymbol{r}$. This $\mathcal{H}_d(\boldsymbol{r})$ term amounts to a coupling between the $4f$ quadrupoles and the deviation $\boldsymbol{r}$ from the cage center:

$$\mathcal{H}_d(\boldsymbol{r}) = -D^{\gamma}\left[(3z^2 - r^2)O_2^0 + 3(x^2 - y^2)O_2^2\right] - D^{\varepsilon}[xy\,\mathcal{P}_{xy} + yz\,\mathcal{P}_{yz} + zx\,\mathcal{P}_{zx}], \quad (5)$$

where x, y, and z are the components, along the cubic axes, of the displacement $\boldsymbol{r}$ of the rare-earth nucleus from the center of the cage. $\{O_2^0, O_2^2\}$ and $\{\mathcal{P}_{xy}, \mathcal{P}_{yz}, \mathcal{P}_{zx}\}$ are the quadrupolar operators transforming, respectively, as the γ (Γ_3) and ε (Γ_5) cubic representations. In the $J = 5/2$ manifold of the Ce^{3+} ion, they are conveniently written in terms of Stevens equivalents [22]. D^{γ} and D^{ε} are constants that, within a representation, define the magnitude of the coupling of the $4f$ quadrupoles with the environment. At a given position $\boldsymbol{r}$

inside the cage, the time independent Schrödinger equation is solved by diagonalization of the local crystal field Hamiltonian $\mathcal{H}(\boldsymbol{r}) = \mathcal{H}_0 + \mathcal{H}_d(\boldsymbol{r})$. This yields the local crystal field scheme and the eigenstates with their composition in terms of $|J, m_J\rangle$ vectors. As the rare earth is not fixed at $\boldsymbol{r}$, the crystal field scheme is no longer a stable property of the rare-earth site. Instead, the scheme has a distribution reflecting that of the guest inside the cage potential well. In turn, this spatial dependence of the rare-earth electrostatic energy contributes to this same potential well. This is the mechanism of the centrifugal Jahn-Teller effect, as described in Ref. [21]. However, this crystal field contribution is a small correction to the main, nonmagnetic, potential term responsible for an energy separation of $\hbar\omega_0/k_B \approx 150$ K between the vibration levels. In the following, the cage potential well is therefore considered unaltered by the CEF correction and, consequently, temperature independent. The individual vibrational states of a rare earth inside a cage are then also temperature independent. As phonons become thermally excited, these stationary states get mixed. However, at temperatures below 50 K, only low frequency phonons get populated: The rare-earth distribution inside the cage remains essentially that of the vibrational ground state, the slight equilibrium shifts induced by phonons resulting, on average, in a tiny widening of the distribution. In the following calculations, that apply for low temperatures, the only considered rare-earth distribution is that of the unperturbed cage vibrational ground state, thus neglecting the Jahn-Teller correction and the interference of excited vibrational states.

B. Vibrational ground state distribution

With a position dependent crystal field scheme, describing the properties of the paramagnetic state requires knowledge of the rare-earth distribution inside the cage. There is no direct and precise experimental determination of this distribution: Spectroscopic or diffraction approaches all require some modeling or intrinsically lack precision. As regards the spectroscopy, for a given energy separation between the lowest vibration levels, the simplest, cubic or higher symmetry, potential wells all result in similar distributions for the singlet ground state. For consistency with the phonons dispersion analysis, we will stick with the harmonic approximation. In this hypothesis, the Gaussian wave function of the singlet ground state is entirely defined by the frequency ω_0 and the mass m of the rare earth. The associated distribution reads as

$$\rho_0(\boldsymbol{r}) = \left(\frac{m\omega_0}{\hbar\pi}\right)^{3/2} e^{-\frac{m\omega_0 r^2}{\hbar}} \tag{6}$$

for which the full width at half maximum is $w_{\mathrm{HM}} = 2\sqrt{\hbar \ln 2/m\omega_0}$. Using the INS value $\hbar\omega_0 = 12.7$ meV and the mass of Ce, one obtains $w_{\mathrm{HM}} \simeq 0.08$ Å for CeB_6. This amounts to the order of magnitude of an average $4f$ shell radius and cannot, in relative terms, be neglected [21]. Then, at temperature T, the paramagnetic value $\widetilde{\mathcal{A}}(T)$ of an observable $\mathcal{A}$ of the rare-earth ion is the cage average:

$$\widetilde{\mathcal{A}}(T) = \iiint_V \rho_0(\boldsymbol{r})\, \langle \mathcal{A}(\boldsymbol{r})\rangle_T \, d^3r, \tag{7}$$

where $\langle \mathcal{A}(\boldsymbol{r})\rangle_T$ is the statistical value of $\mathcal{A}$ at position $\boldsymbol{r}$. Despite the rare-earth movement, thanks to the ergodic hypothesis, this value can be considered as a local time average. Alternatively, as there are as many instances of the $\boldsymbol{r}$ position, as there are identical cages in the paramagnetic crystal, a statistical ensemble is realized: $\langle \mathcal{A}(\boldsymbol{r})\rangle_T$ becomes a macroscopic variable. The same applies to the spatial average $\widetilde{\mathcal{A}}(T)$ for which Eq. (7) is a convenient local definition. In principle, the volume V of the integral should be infinite, but it can be restricted to the cage extension without significant incidence on the $\widetilde{\mathcal{A}}(T)$ value. This requires adapting the normalization of $\rho_0(\boldsymbol{r})$ to the retained volume. Here the chosen V volume is a cube of edge $a = 0.3$ Å, which is more than three times the FWHM of the distribution. In a numerical implementation of the sum of Eq. (7), one can take advantage, as in the calculation of the phonons specific heat, of the cubic symmetry. This is achieved by restricting to samples in V that belong to a representative volume, analog in direct space to the tetrahedron of Fig. 4. The numerical results that follow are obtained by considering 286 independent samples (i.e., positions where the Hamiltonian is diagonalized and local observables produced), that represent a total of 9261 samples in V.

C. Calculation of the thermodynamic functions

At each sample position $\boldsymbol{r_s}$ inside the volume V, the total crystal field Hamiltonian $\mathcal{H}_{\mathrm{CEF}}(\boldsymbol{r_s}) = \mathcal{H}_0 + \mathcal{H}_d(\boldsymbol{r_s})$ has to be numerically diagonalized. Then, at a given temperature T, from the local partition function $Z(T, \boldsymbol{r_s})$, the local internal and free energies are derived, as well as the associated entropy. The cage averages are then computed, according to the above described method. This procedure requires a value for the fourth order B_4 CEF parameter that defines the cubic $\mathcal{H}_0$ crystal field Hamiltonian [23] and two other values, D^γ and D^ε, for the displacement-quadrupoles coupling constants of $\mathcal{H}_d$. The value $B_4 = -1.47$ K is known from the Raman and INS investigation [10], the negative sign yielding a Γ_8 ground state. There is no such experimental determination for the D^γ and D^ε parameters, here introduced for describing the cage splitting of the Γ_8 level. One predicted consequence of this splitting in an anomalous variation of the magnetic entropy in the paramagnetic range [21], as the one observed in CeB_6. Here it is assumed that this anomaly is entirely due to a cage split Γ_8. Within this assumption, the values for D^γ and D^ε are those that best describe the observed temperature variation of CeB_6 entropy. From guessed initial values for D^γ and D^ε, a least-squares approach was used for optimizing the description of the entropy data in the 4–20 K temperature range (see Fig. 6). In order to speed up the optimization process, only four experimental points, at $T = 4$, 10, 12.5, and 20 K, were used for defining the $S_Q(D^\gamma, D^\varepsilon)$ sum of squared differences to be minimized. This search points to four sets of parameters, reported in Table I, along with their associated S_Q values.

In Fig. 7 the magnetic entropy variations, computed using the sets of values in Table I, are compared with our experimental data. Despite an advantage to the sets with negative D^ε, in terms of S_Q values, at the graph's scale, the four sets result in indistinguishable lines. They all satisfactorily describe the observed variation of CeB_6 entropy in the paramagnetic range. All the zero temperature limits are very close to $R \ln 2$. This

TABLE I. Table of the retained sets of D^{γ} and D^{ε} values that best describe the paramagnetic variation of CeB_6 magnetic entropy. The optimization is based on the minimization of S_Q, the sum of the squared differences, between experiment and calculation, at four selected temperatures (see text). The sets are named by reference to the respective signs of the parameters.

Set	D^{γ} (K/Å^2)	D^{ε} (K/Å^2)	S_Q [J^2/(K^2 mol^2)]
++	+104.1	+3536	3.95×10^{-4}
+−	+75.6	−4878	2×10^{-4}
−+	−107.8	+3610	2.87×10^{-4}
−−	−98.7	−4381	1.3×10^{-4}

corresponds to the expected Kramers minimal degeneracy for Ce^{3+}. In the model we use, the fourfold degeneracy of the Γ_8 level is realized only for a Ce ion at the very center of the cage, which has vanishing weight in the cage averaged values (cf. the distribution in Fig. 8, lower part). At all locations outside the center, the Γ_8 quadruplet is split into two doublets. At 0 K, only the lowest local doublet is populated, with corresponding magnetic entropy.

The upper parts of Fig. 8 show the dependencies of the CEF levels as function of the displacement along the two crystallographic directions: Fourfold (left) and threefold (right). The two quadrupolar cubic representations are thus separated, D^{γ} and D^{ε} being, respectively, active for the fourfold axis and threefold axis. Along a fourfold axis, the splitting of the Γ_8 level has the simplest structure, with a symmetrical energy separation of the two resulting doublets. At the scale of the graph, the upper Γ_7 doublet appears unaffected. The splitting scheme along a threefold axis differs on that point, with a substantial interference of the Γ_7 level at distances greater than 0.05 Å from the center. In particular, for a

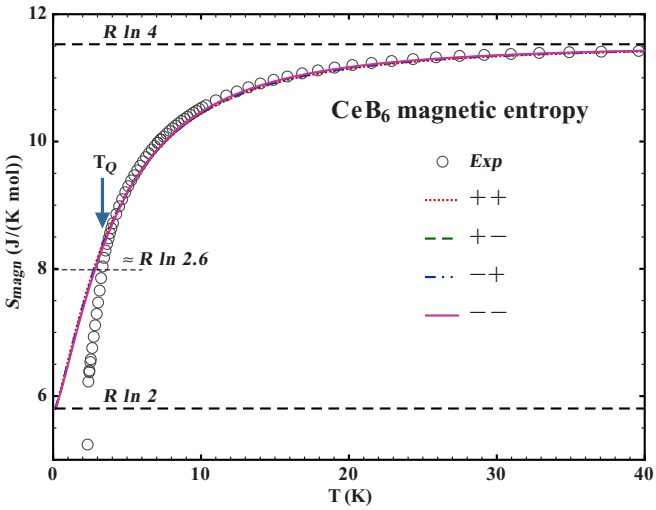

FIG. 7. Experimental (circles) and computed variations (lines) of CeB_6 magnetic entropy for the D^{γ} and D^{ε} sets from Table I. At the graph scale, the computed curves are indistinguishable. The horizontal, dashed lines give the reference values for a doublet and quadruplet. The shorter dashed line at $\approx R \ln 2.6$ points to the experimental value at T_Q.

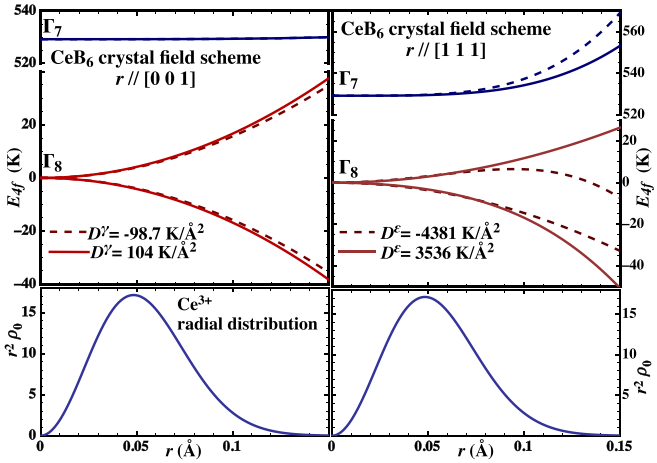

FIG. 8. Cage splitting of the central CEF scheme as result of a displacement $\boldsymbol{r}$ along a fourfold axis (upper left) or threefold axis (upper right). The active quadrupole-displacement coupling constants are, respectively, D^{γ} and D^{ε}. Note that the vertical energy axes are sliced in order to simultaneously display the energies for the Γ_8 and Γ_7 levels. The graphs show the effect of D^{γ}, respectively D^{ε}, values with opposite signs, from the sets "++" and "−−" in Table I. Lower parts: Duplicate radial distributions of Ce^{3+} for the vibrational harmonic ground state, using $\hbar\omega_0 = 12.7$ meV.

negative D^{ε}, which corresponds to the best agreement with the entropy results, the mixing between the Γ_7 and Γ_8 states induces a strong "repulsion" of the split levels. At distances r above 0.1 Å, the doublets originating from the Γ_8 plunges to lower energies, while the Γ_7 goes up. However, the actual consequences of this modified CEF scheme are mitigated by the distribution of the Ce^{3+} ion (see Fig. 8, lower part), which limits the contribution of distances above 0.1 Å. The influence of the cage split CEF scheme mainly results from the splitting of the Γ_8 level for distances r around 0.05 Å, where, for the retained D^{γ} and D^{ε} values, the splitting is of similar amplitude (about 8 K) for these two displacement directions.

Figure 9 shows the paramagnetic variation of the internal magnetic energy. The four computed curves correspond to the set of parameters of Table I that optimally describe the entropy thermal dependence. They are vertically shifted in order to have zero internal energy at 0 K. The experimental curve (circles in Fig. 9), obtained by numerical integration of the magnetic part of the specific heat, is also shifted in order to be superimposed with the computed variations. Without surprise, the theoretical descriptions show an agreement of similar quality as observed for the entropy. The well separated Γ_7 level having negligible influence in the considered temperature range, the dependence of the computed internal energy essentially reflects the Boltzmann population of CEF states originating from the Γ_8 ground state. The energy curves actually follow the shift of the barycenter of the split Γ_8 level. This differs from the unsplit and unpopulated Γ_7 level. Its energy barycenter does not depend on the temperature (see Fig. 8, upper part), but only on the cage distribution of Ce^{3+}. Consequently, as the temperature is lowered below 50 K, the average energy separation between the Γ_8 and Γ_7 levels increases, reflecting the reduction in the average Γ_8 energy.

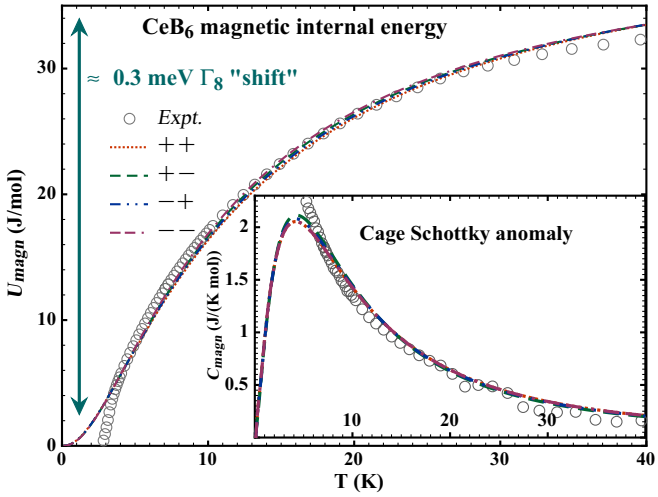

FIG. 9. Experimental (circles) and computed (lines) temperature variations of the magnetic internal energy, for the sets of D^{γ} and D^{ϵ} values in Table I. The chosen origin for the computed curves is zero energy at 0 K. The experimental data are, accordingly, vertically shifted. This energy variation is indicative of an overall ≈0.3 meV "shift" in the average energy of the Γ_8 level. The inset shows the corresponding specific heat curves. The computed ones are obtained from numerical derivation and show the cage Schottky anomaly.

This is, in effect, what has been observed via Raman and INS scattering [10,24] that reveal an increase in the energy transfer between the two CEF levels. However, a quantitative examination shows a discrepancy between our calculations that yield a shift of approximately 0.3 meV (see Fig. 9), and the scattering experiments that point to a larger 1 meV value. It seems that a reduction in the Γ_8 energy, consistent with the specific heat results, cannot entirely account for the increase in the $\Gamma_8 - \Gamma_7$ separation. Simultaneously, with the Γ_8 level lowering, this would require a higher average Γ_7 level as the temperature is reduced. As shown in Fig. 8, right upper frame, this could be obtained in case of an increased probability of the presence of the Ce^{3+} ion along the threefold axes, beyond $r = 0.1$ Å. Such a Ce^{3+} distribution challenges both our assumptions of a simple harmonic oscillator ground state and of a negligible centrifugal Jahn-Teller effect.

Another possible fault in our analysis is the confusion between the $\Gamma_8 - \Gamma_7$ average energy separation and the peak position in the Raman or INS scattering experiments. This supposes that the scattering probability is independent of the Ce^{3+} position in the cage. In case of enhanced transition probabilities for peripheral positions, the scattering peak would display, in agreement with the upper part of Fig. 8, a shift larger than expected from the simple average $\Gamma_8 - \Gamma_7$ separation. The inset of Fig. 9 shows the computed magnetic specific heat curves, deduced from the internal energy variations, that display a characteristic Schottky anomaly, as predicted in Ref. [21]. They are superimposed with the magnetic specific heat experimental data (circles). The cage split Γ_8 level accounts well for the increase in the specific heat as the temperature falls below 40 K. Contrary to the usual CEF Schottky anomalies that result from the proximity of discrete CEF levels, the cage Schottky anomaly starts with a steep slope at 0 K. This reflects the continuum of available energy levels that result from the split central CEF ground state. In the case of CeB_6, the orderings at T_Q and T_N dominate the low temperature part of the specific heat: No Schottky peak is visible in the experimental data, but the excess of specific heat above T_Q could correspond with the flank of the expected anomaly.

IV. SUMMARY AND DISCUSSION

A. The nature of the transition at T_N

This study follows a long series of investigations of the CeB_6 compound. Thanks to new specific heat measurements, the process of the antiferromagnetic transition has been detailed. The temperature profiles across T_N are consistent with a first-order process, involving a latent heat of about 1.30 J/mol. Part of the missing paramagnetic entropy of CeB_6 is thus recovered at T_N.

In the temperature variation of CeB_6 physical properties, the first-order transition should reflect as a discontinuity at T_N, between the so-called antiferroquadrupolar (phase II) and antiferromagnetic (phase III) phases. For instance, resistivity, volume, and ordered magnetic moment should display a jump at T_N. From measurements on single crystals, the volume [7,25] and resistivity [2,26] display abrupt anomalies at T_N. From the published data, whether these quantities are continuous or discontinuous at T_N could be discussed at length. One has to consider that, below T_N, the system is no longer cubic, but tetragonal [7]: The domains may differently contribute to a macroscopic quantity, possibly mitigating a discontinuity at T_N. Also, one cannot expect a spectacular discontinuity since the jump in the entropy at T_N represents less than 10% of the total entropy variation in the antiferromagnetic range.

As regards the first-order magnetic susceptibility, it is clearly anisotropic [7,27] below T_N in agreement with the tetragonal symmetry. In case of a second-order Néel point, this anisotropy should progressively cancel as T_N is approached and the cubic symmetry restored. This prediction is contradicted by the experiments, especially when domains effects [7] are dealt with: Clear discontinuities are observed at T_N for the susceptibilities along the threefold and twofold axes.

Looking at microscopic probes, there is published data showing the crossing of T_N via neutron or x-ray diffraction. In Ref. [28], the thermal dependence of two antiferromagnetic powder neutron reflections is shown with no evident discontinuity at T_N. Due to the boron absorption, the intensities are weak. It is difficult in such conditions to decide at which temperature the intensity cancels, with a reported $T_N = 2.8$ K against a more common $T_N = 2.3$ K, and whether the process is continuous or not. X-ray single crystal data provide an alternative insight with the temperature dependence of $[\frac{1}{2}\ \frac{1}{2}\ \frac{1}{2}]$ related nonresonant charge reflections. These reflections are nonzero in both phases II and III, which helps identifying a possible discontinuity. In Refs. [29,30], the reported dependencies show a sharp anomaly at T_N, with a clear discontinuity in the graph of Ref. [30].

If, after this scrutiny, uncertainties are left as regards the nature of the antiferromagnetic transition in CeB_6, the decisive evidence should come from the thermodynamical

analysis. The here reported temperature profiles, while heating up the sample across T_N, show a plateau which can be quantitatively associated with an amount of heat required to achieve the transition. This is consistent with a first-order transition.

A first-order transition at T_N allows reconsidering the relationship between phases II and III. While it is generally considered that the antiferromagnetism of CeB_6 develops over the paramagnetic, charge organization of phase II [3], some difficulty emerges when considering the detail of the antiferromagnetic structure. The proposed structures for phase III are multiaxial [3,31], with magnetic moments along twofold axes. This contradicts the simplest, Landau or mean-field, descriptions of a second-order magnetic ordering. Indeed, for a magnetic ion at a site of cubic symmetry, the low field anisotropy reflects the single-ion third-order magnetic susceptibility that favors fourfold or threefold axes [32]. The twofold axes cannot be the easy ones, unless a discontinuous transformation occurs that involves higher order susceptibilities at T_N. In case of a first-order transition at T_N, there is no such contradiction. More generally, removing the continuity condition between phases II and III allows for more options to be considered as regards the mysterious nature of phase II.

B. The magnetic entropy below T_Q

Other valuable information can be extracted from the low temperature part of the experimental entropy curve (inset of Fig. 6). It can be seen that, within phase II, from T_Q to T_N, the magnetic entropy decreases from 8 to 6.2 J/(K mol). This leads, despite the entropy correction of the first-order transition, to an entropy value for phase II at T_N that only slightly exceeds $R\ln 2 = 5.8$ J/(K mol). If phase II were, as reported, nonmagnetic, its 0 K extrapolated entropy value should be close to that of a doublet, i.e., $R\ln 2$. This is the Kramers theorem applied to a Ce^{3+} ion. In case of a simple, antiphase, magnetic order, the extrapolated entropy value would be zero, as for phase III. Looking at the inset of Fig. 6, it is likely that the 0 K extrapolated value for phase II is much smaller than $R\ln 2$, but still larger than 0. This intermediate value adds to the peculiarity of phase II and puts into question its nonmagnetic nature. If the ordering mechanism for phase II were indeed nonmagnetic, a 0 K extrapolated entropy value much lower than $R\ln 2$ is, at least, indicative of strong magnetic correlations. Evidence for magnetic correlations within phase II have been previously obtained from polarized neutron scattering experiments [33], indicative of short-range magnetic arrangements with $[\frac{1}{2}\ \frac{1}{2}\ \frac{1}{2}]$ wave vector. Another mechanism that may lower the entropy below the Kramers' minimum is the Kondo coupling (cf. last paragraph).

C. The entropy in the paramagnetic range

The calculation of the phonons contribution to the specific heat of hexaborides, based on a better account of the cage system dispersion curves, yields a satisfactory description for LaB_6. It shows that, at temperatures below 50 K, it is the cage oscillator frequency that is the main determinant of the changes across the series. No simple method allows extrapolating from one element to another: An experimental determination is required. In the case of CeB_6, the used value is derived from the phonons' dispersion curves obtained from inelastic neutron scattering. Thanks to the correction introduced by the first-order magnetic transition and to this improved description of the phonon contribution, an improved experimental determination of CeB_6 magnetic entropy has been obtained. The temperature variation of this entropy displays the paramagnetic plateau characteristic of the fourfold degenerate Γ_8 CEF ground state. This plateau does not materialize immediately above the ordering temperature, but for temperatures higher than 30 K. This is ten times higher than the ordering temperature of CeB_6 and unlikely to relate to pair correlations.

1. The cage crystal field interpretation

The temperature scale of the abnormal thermal evolution of CeB_6 paramagnetic entropy fits with another peculiarity of this compound: As evidenced from Raman and thermal neutrons scattering, the $\Gamma_8 - \Gamma_7$ CEF excitation shifts towards higher energies below 20 K. In the cage context, with an orbitally degenerate central CEF ground state, both the entropy and spectroscopy anomalies can be related to a single mechanism: the dynamical splitting of the CEF ground state as a result of the rare-earth movement. An attempt, based on this crystal field mechanism, at describing the entropy anomaly of CeB_6 is satisfactory, at the price of the introduction of two parameters describing the CEF change for an offset Ce^{3+}. An associated shift with the temperature of the CEF $\Gamma_8 - \Gamma_7$ excitation is predicted, the simplest estimate yielding about one third of the reported value. However, as the computed values, confronted with the experimental data, result from Boltzmann and spatial averages, there is some intrinsic indetermination in this CEF description. In the case of CeB_6, at least four sets of parameters are consistent with the specific heat data. Additional experimental data may allow us to distinguish between them, but this also requires some theoretical effort in order, for instance, to describe experiments under an applied magnetic field. The first magnetic field effect one might consider is the emergence of a magnetization, reflecting the first-order magnetic susceptibility. In the case of CeB_6, this might be inconclusive. Indeed, however effective it might be in the description of the zero field thermodynamical anomalies, the cage crystal field model cannot significantly improve the description of the first-order magnetic susceptibility. As illustrated in Ref. [21], in case the CEF ground state splits inside the cage into magnetic doublets, only a small correction to the magnetic susceptibility is to be expected. Moreover, a description of CeB_6 paramagnetic susceptibility, based on the known crystal field complemented with exchange couplings, is far from satisfactory in face of the published temperature dependencies of the inverse magnetic susceptibility [1,34]: Up to room temperature, the computed CEF susceptibility is 10% to 15% smaller than the experimental one, which forces to use extravagantly large values for the negative exchange coupling constant. It seems that the measured susceptibility includes a significant contribution from the conduction electrons, opposite to that of the Ce^{3+} ion, and no CEF based model can account for that. Another test of the cage crystal field

interpretation would be to look for signatures of the associated centrifugal Jahn-Teller effect [21]. This effect has direct, but moderate, consequences on the system volume and vibration frequency of the rare earth. In CeB_6, as for two other rare-earth hexaborides with non-Kramers CEF ground states, PrB_6 and NdB_6, the thermal expansion coefficients deduced from x-ray diffraction [35] display a minimum in the paramagnetic range, slightly below 20 K. These x-ray results are consistent with the low temperature thermal expansion investigation of CeB_6 and $Ce_xLa_{1-x}B_6$ crystals [36]: CeB_6's linear thermal expansion coefficient $\alpha(T)$ significantly decreases from T_Q down to a minimum close to $T = 15$ K. At lower Ce concentration, in addition to this minimum, a maximum in $\alpha(T)$ can be discerned just below 5 K. The authors of Ref. [36] have ascribed this thermal expansion anomaly to the Kondo effect. The cage CEF scenario provides an alternative interpretation, in the form of the centrifugal Jahn-Teller effect and its natural lattice consequences: Unlike the Kondo coupling, CEF effects directly involve the crystal's charge distribution. As regards the Jahn-Teller changes in the oscillator frequency, a softening of associated phonons in the percent range is expected [21]. Its detection requires high resolution, infrared or neutron, spectroscopic techniques. Presently, there are no available experimental results fulfilling these requirements.

2. On the interference of the Kondo coupling

CeB_6 is often referred as an archetypical Kondo lattice system, a logarithmic dependence and minimum being observed in the temperature variation of the resistivity [26]. The reported values for the Kondo temperature T_K are fairly low [2], below 10 K, which means that the screening of the Ce^{3+} spin is ineffective down to low temperatures in the paramagnetic range. This is confirmed at lower temperature by the antiferromagnetic ordering, which attest to the dominance of the RKKY interactions over the Kondo coupling. Instead of the here considered cage-split Γ_8 CEF ground state, one could tentatively ascribe the excess of specific heat in the low-temperature range to the Kondo coupling. This requires complex theoretical treatments and most of the work in this sense is devoted to the impurity Kondo problem, not to the Kondo lattice. Theoretically [37,38], a specific heat peak is predicted, reflecting the screening of the Ce^{3+} spin and the associated reduction of the magnetic entropy. The peak is centered around T_K and, on a logarithmic temperature scale, extends over two decades. There is available experimental data, obtained from measurements on dilute $Ce_xLa_{1-x}B_6$ systems, that can be compared with these impurity models [39,40]. In these systems, a specific heat peak is indeed observed at low temperature, close to the estimated T_K of about 1 K, on which the authors of Refs. [39,40] adjusted the Kondo impurity models' peaks. The entropy variations in the low temperature range, as computed from the experimental specific heat peak or from its adjusted theoretical description, remain below $R \ln 3$ J/(K mol). In order to explain the difference with the quadruplet $R \ln 4$ J/(K mol) value, the authors of both Refs. [39,40] invoke a split Γ_8 level, after the results of Ref. [10]. Extrapolating to the situation of the concentrated CeB_6, one might conclude that, there also, the description of the entropy variation requires accounting for the split Γ_8. This is precisely the basis of the cage CEF model. Both models can account, at least partially, for the low-temperature entropy variation. The crystal field model cannot totally lift the magnetic degeneracy, but only the orbital part, yielding a minimum $R \ln 2$ J/(K mol) magnetic entropy. In principle, the Kondo coupling can, as the RKKY couplings in CeB_6, completely lift the degeneracy. These two approaches are actually nonindependent, nor exclusive, and the best model would encompass both the cage CEF and Kondo coupling. Evidently, this would represent a considerable theoretical undertaking.

ACKNOWLEDGMENTS

The authors would like to thank Dr. N. Y. Shitsevalova and collaborators, from the IPMS in Kiev, Ukraine who prepared the LaB_6 single crystals. We are grateful to Dr. L.-P. Regnault from CEA, INAC in Grenoble, France, for lending us the CeB_6 crystals and exchanging views on the CeB_6 puzzle. We also thank Dr. C. Lacroix, Institut Néel, for her critical reading of the manuscript and precious advices on the Kondo topic.

[1] M. Kawakami, S. Kunii, T. Komatsubara, and T. Kasuya, Solid State Commun. **36**, 435 (1980).
[2] A. Takase, K. Kojima, T. Komatsubara, and T. Kasuya, Solid State Commun. **36**, 461 (1980).
[3] J. Effantin, J. Rossat-Mignod, P. Burlet, H. Bartholin, S. Kunii, and T. Kasuya, J. Magn. Magn. Mater. **47–48**, 145 (1985).
[4] K. Hanzawa and T. Kasuya, J. Phys. Soc. Jpn. **53**, 1809 (1984).
[5] W. A. C. Erkelens, L. P. Regnault, P. Burlet, J. Rossat-Mignod, S. Kunii, and T. Kasuya, J. Magn. Magn. Mater. **63-64**, 61 (1987).
[6] M. Takigawa, H. Yasuoka, T. Tanaka, and Y. Ishizawa, J. Phys. Soc. Jpn. **52**, 728 (1983).
[7] M. Amara and R.-M. Galéra, Phys. Rev. Lett. **108**, 026402 (2012).
[8] N. Ali and S. B. Woods, J. Appl. Phys. **57**, 3182 (1985).
[9] H. Hacker, Y. Shimada, and K. S. Chung, Phys. Status Solidi A **4**, 459 (1971).
[10] E. Zirngiebl, B. Hillebrands, S. Blumenröder, G. Güntherodt, M. Loewenhaupt, J. M. Carpenter, K. Winzer, and Z. Fisk, Phys. Rev. B **30**, 4052 (1984).
[11] T. Fujita, M. Suzuki, T. Komatsubara, S. Kunii, T. Kasuya, and T. Ohtsuka, Solid State Commun. **35**, 569 (1980).
[12] Y. Peysson, C. Ayache, J. Rossat Mignod, S. Kunii, and T. Kasuya, J. Phys. **47**, 113 (1986).
[13] K. N. Lee and B. Bell, Phys. Rev. B **6**, 1032 (1972).
[14] Y. B. Paderno, V. I. Lazorenko, and A. V. Kovalev, Sov. Powder Metall. Met. Ceram. **20**, 717 (1981).
[15] T. Tanaka, E. Bannai, S. Kawai, and T. Yamane, J. Cryst. Growth **30**, 193 (1975).
[16] J. S. Hwang, K. J. Lin, and C. Tien, Rev. Sci. Instrum. **68**, 94 (1997).

[17] J. Hofmann, A. Paskin, K. Tauer, and R. Weiss, J. Phys. Chem. Solids **1**, 45 (1956).
[18] H. G. Smith, G. Dolling, S. Kunii, M. Kasaya, B. Liu, K. Takegahara, T. Kasuya, and T. Goto, Solid State Commun. **53**, 15 (1985).
[19] S. Kunii, J. M. Effantin, and J. Rossat-Mingnod, J. Phys. Soc. Jpn. **66**, 1029 (1997), .
[20] D. Mandrus, B. C. Sales, and R. Jin, Phys. Rev. B **64**, 012302 (2001).
[21] M. Amara, Phys. Rev. B **99**, 174405 (2019).
[22] K. Stevens, Proc. Phys. Soc. (London) A **65**, 209 (1952).
[23] P. Morin and D. Schmitt, *Quadrupolar Interactions and Magnetoelastic Effects in Rare Earth Intermetallic Compounds* (Elsevier Science, Amsterdam, 1990), Chap. 1, pp. 1–132.
[24] M. Loewenhaupt, J. Carpenter, and C.-K. Loong, J. Magn. Magn. Mater. **52**, 245 (1985).
[25] T. Nakajima, S. Kunii, T. Komatsubara, and T. Kasuya, J. Magn. Magn. Mater. **15-18**, 967 (1980).
[26] K. Winzer and W. Felsch, J. Phys. Colloq. **39**, C6-832 (1978).
[27] S. Horn, F. Steglich, M. Loewenhaupt, H. Scheuer, W. Felsch, and K. Winzer, Z. Phys. B Condens. Matter **42**, 125 (1981).
[28] J. Rossat-Mignod, P. Burlet, T. Kasuya, S. Kunii, and T. Komatsubara, Solid State Commun. **39**, 471 (1981).
[29] F. Yakhou, V. Plakhty, H. Suzuki, S. Gavrilov, P. Burlet, L. Paolasini, C. Vettier, and S. Kunii, Phys. Lett. A **285**, 191 (2001).
[30] Y. Tanaka, U. Staub, K. Katsumata, S. W. Lovesey, J. E. Lorenzo, Y. Narumi, V. Scagnoli, S. Shimomura, Y. Tabata, Y. Onuki, Y. Kuramoto, A. Kikkawa, T. Ishikawa, and H. Kitamura, Europhys. Lett. **68**, 671 (2004).
[31] O. Zaharko, P. Fischer, A. Schenck, S. Kunii, P.-J. Brown, F. Tasset, and T. Hansen, Phys. Rev. B **68**, 214401 (2003).
[32] P. Morin and D. Schmitt, Phys. Rev. B **27**, 4412 (1983).
[33] V. P. Plakhty, L. P. Regnault, A. V. Goltsev, S. V. Gavrilov, F. Yakhou, J. Flouquet, C. Vettier, and S. Kunii, Phys. Rev. B **71**, 100407(R) (2005).
[34] N. E. Sluchanko, A. V. Bogach, V. V. Glushkov, S. V. Demishev, V. Y. Ivanov, M. I. Ignatov, A. V. Kuznetsov, N. A. Samarin, A. V. Semeno, and N. Y. Shitsevalova, J. Exp. Theor. Phys. **104**, 120 (2007).
[35] V. Novikov, E. Pilipenko, and S. Bud'ko, Solid State Commun. **252**, 51 (2017).
[36] R. Schefzyk, M. Peschke, F. Steglich, and K. Winzer, J. Magn. Magn. Mater. **63–64**, 67 (1987).
[37] K. Schotte and U. Schotte, Phys. Lett. A **55**, 38 (1975).
[38] V. T. Rajan, J. H. Lowenstein, and N. Andrei, Phys. Rev. Lett. **49**, 497 (1982).
[39] N. Sato, M. Takahashi, T. Kashima, K. Sugiyama, M. Date, T. Satoh, and T. Kasuya, J. Magn. Magn. Mater. **52**, 250 (1985).
[40] H. Gruhl and K. Winzer, Solid State Commun. **57**, 67 (1986).